MULTIMODAL IMAGING OF DENDRITIC CELLS USING A NOVEL HYBRID MAGNETO-OPTICAL NANOPROBE

Patrick S. Mackay[a], **Gert-Jan Kremers, PhD**[b], **Saho Kobukai, PhD**[a], **Jared G. Cobb, MS**[a,d], **Alex Kuley**[a], **Sandra J. Rosenthal, PhD**[c], **Dmitry S. Koktysh, PhD**[*,c], **John C. Gore, PhD**[a,d,e], and **Wellington Pham, PhD**[*,a,d,e]

[a]Vanderbilt University, Institute of Imaging Science, Nashville, Tennessee, USA

[b]Department of Molecular Physiology and Biophysics

[c]Department of Chemistry, Vanderbilt Institute of Nanoscale Science and Engineering

[d]Department of Biomedical Engineering

[e]Department of Radiology and Radiological Sciences

Abstract

A transfecting agent-coated hybrid imaging nanoprobe (HINP) comprised of visible and near-infrared (NIR) light emitting quantum dots (QDs) tethered to superparamagnetic iron oxide (SPIO) nanoparticles was developed. The surface modification of QDs and SPIO particles and incorporation of dual QDs within the SPIO were characterized by dynamic light scattering (DLS), quartz crystal microbalance (QCM) analysis and atomic force microscopy (AFM). The optical contrasting properties of HINP were characterized by absorption and photoluminescence spectroscopy and fluorescence imaging. Multicolor HINP was used in imaging the migration of dendritic cells (DCs) by optical, two-photon and magnetic resonance imaging techniques.

Keywords

Molecular Imaging; Dendritic cells; Nanotechnology; Magnetic Resonance Imaging

Background

In the past decade, major advances have occurred in the development and implementation of noninvasive imaging technologies for biomedical research, especially, optical[1–7] and magnetic resonance (MR)[8–10] imaging. These imaging techniques have had considerable impact on the way we detect and characterize diseases in both basic research and clinical applications. Despite such success, it has become increasingly apparent that often no single imaging modality can effectively provide information, and that different modalities each have complementary advantages and limitations. Therefore, one current trend in this area is

*Corresponding author: Tel: (615) 936-7621. dmitry.koktysh@Vanderbilt.Edu. * wellington.pham@vanderbilt.edu .

to try to combine different imaging modalities by using multimodal molecular probes that provide imaging information greater than that obtainable by any single approach[11, 12]. This has a profound implication for cell tracking, particularly in research that focuses on tracking the migration of dendritic cells (DCs). Optical imaging facilitates the ability to decipher specific cellular and molecular interactions of DCs in the microenvironment within the lymphoid tissue, whereas MR imaging serves as the preferred modality for tracking the global distribution of cells in the lymph nodes (LNs) due to its high soft-tissue contrast and spatial resolution[13]. In a dual approach, optical and MR imaging techniques can be used in a complementary fashion to pinpoint the distribution of adaptively transferred DCs and determine their fate in vivo with the desired temporal and spatial resolution.

In this work, we report the development of a hybrid nanoprobe (HINP) to track DCs using optical and MR imaging. The HINP consists of both visible and near-infrared (NIR) emitting semiconductor quantum dots (QDs) tethered to superparamagnetic iron oxide (SPIO) nanoparticles. Additionally, the resultant complex was encapsulated with a transfecting reagent on the surface to facilitate cell uptake. Preliminary data demonstrated the robust chemistry of HINP, necessary for the incorporation of QDs onto SPIO. The probe is stable and sensitive, and thus enables the tracking of cells in vivo.

Methods

Materials

Cadmium acetate hydrate (99.9%), polyallylamine chloride (PAH) (M.w. 15000), poly-D-lysine hydrobromide (PLL) (M.w. 4000–15000), poly(diallyldimethylammonium chloride) (PDDA) (M.w. 400.000–500.000), and polystyrene sulfonate (PSS) (M.w. 70.000) were purchased from Aldrich, 3-mercaptopropionic acid (MPA) (99%) and mercury acetate (99%) were purchased from Acros Organics and sodium borohydride (98%), tellurium (99.999%), thioacetamide (TAA) (98%), zinc acetate (99.98%) and thiourea (99%) were purchased from Alfa Aesar.

Adult C57BL/6 mice were obtained from the Jackson Laboratory (Bar Harbor, ME) and bred in house. Animal experiments were carried out per the guidelines provided by the Vanderbilt University Institutional Animal Care and Use Committee (IACUC) and the National Institutes of Health Guide for the Care and Use of Laboratory Animals.

Synthesis of visible and NIR QDs

CdTe and CdHgTe QDs were prepared with some modifications from the previously reported procedures[14, 15]. Briefly, Te powder (128 mg, 1mmol) was added to a cool solution of $NaBH_4$ (78 mg, 2 mmol) in water (3mL) purged with argon. The resulting solution of NaHTe was added to another beaker containing 50 mL of degassed water. While a Cd-MPA complex was prepared by adding MPA (26.0 μL, 0.3 mmol) to a solution of cadmium acetate (26.7 mg, 0.1 mmol) in 50 mL of water. Then, the pH was adjusted to 8.5 using 1M NaOH. In another step in the preparation, Hg-MPA was generated in the same manner as Cd-MPA. All the solutions were purged with argon for approximately 30 minutes before use.

CdHgTe or CdTe QDs were prepared by consecutive injections of NaHTe (2.6 mL) and Hg-MPA (3.0 mL) or NaHTe into a Cd-MPA solution, which then was heated to 90°C for 10 minutes. The optical property of the resultant CdHgTe and CdTe QDs were tuned by varying the particle size which were controlled based on the heating time and doped level of Hg.

The core-shell CdTe/CdS and CdHgTe/CdS QDs were prepared by overcoating the synthesized core QDs with CdS[14, 16]. First, we generated the Cd-MPA-TAA precursor by mixing Cd-acetate (66.7 mg) with MPA (65.0 μL) and TAA (19.0 μL), then the pH of the resulting solution was adjusted to 8.5. The product CdS (5.0 mL) was injected dropwise into a 50 mL solution of CdTe or CdHgTe QDs, and the mixture was heated to 90°C for one hour. The products of CdTe/CdS or CdHgTe/CdS QDs were washed from the starting materials with isopropanol. Then, the pure product was isolated via centrifugation and redissolved in water.

Finally, the core-shell CdTe/CdS and CdHgTe/CdS QDs were coated with ZnS using a reported procedure[17, 18]. A Zn-MPA-thiourea precursor was prepared by mixing Zn-acetate (18.0 mg, 0.08 mmol) with MPA (21 mL, 0.2 mol) and thiourea (15 mg, 0.2 mmol) in 5.0 mL water. The resultant ZnS was adjusted to a pH of 11.5 before being injected into the QD solution, and the mixture was heated to 80°C for 45 minutes under the presence of argon. The final products of CdTe/CdS/ZnS and CdHgTe/CdS/ZnS QDs were purified to remove unreacted precursors in the same manner described for the CdTe/CdS or CdHgTe/CdS QDs.

Assembling QDs onto SPIO

The incorporation of QDs onto SPIO was achieved by employing the electrostatic assembling approach[19, 20]. PAH (50 μL, 10 mg/mL in 0.15 M NaCl, pH=5) was added dropwise with vigorous stirring into a solution of SPIO-DX nanoparticles (0.5 mL) which our laboratory developed and reported[13] (1mg/mL in 0.15 NaCl, pH=5). After stirring for 15 minutes, the SPIO-DX-PAH nanoparticles were collected and washed (3×) with 0.15 M NaCl to remove unreacted materials using a microfilter (Microcon, YM-100, cut off of 100,000) at 10,000 rpm for 12 minutes. The product was redispersed in 0.5 mL water.

The solution of SPIO-DX-PAH was added to a mixture of visible and NIR QDs in water (1.0 mL each, pH=9) while stirring vigorously for 20 minutes. The resulting SPIO-DX-PAH-QD product was collected and washed with water (3×) using a microcentrifuge technique as described above before being redispersed in 0.5 mL of PBS. To coat the final probe with the transfecting reagent PLL, we added the SPIO-DX-PAH-QDs solution to a PLL solution (6 μL, 1 mg/mL) with vigorous stirring. The final product was collected, washed and redispersed in 0.5 mL of PBS at pH 7.4 before imaging application.

HRTEM was performed on a Philips CM20 TEM, and atomic force microscopy (AFM) images were obtained using a Nanoscope IIIa (Veeco). The AFM samples were prepared by assembling nanoparticles into a silicon wafer with either a PDDA layer or PDDA/PSS bilayer adapted from a reported procedure[21, 22]. The absorption spectra of nanoparticles were recorded on a Cary 5000 UV-vis-NIR spectrometer (Varian). The photoluminescence spectra were obtained from a Fluorolog-3 FL3-111 (Jobin Yvon/Horiba).

The probe assembly was investigated using the QCM method (RQCM, Maxtek Inc.) with the quartz crystal resonator operating at a frequency of 5 MHz. The hydrodynamic diameter of nanoparticles and their zeta potential were determined using a Zetasizer Nano ZS (Malvern Instruments, UK). ImageJ (NIH) was used to process and analyze the captured images.

Dendritic cells and toxicity study

DCs were isolated from the bone marrow of C57BL/6 mice as described in the past[13, 23]. Briefly, bone marrow precursors were flushed out with RPMI from femurs and tibias of mice and subsequently processed into a single cell suspension using a 70-mm mesh strainer. Erythrocytes were lysed with 0.83% ammonium chloride with 2 minutes of incubation at room temperature. The cells were centrifuged for 5 minutes at 300 g and washed twice in

RPMI. After the washes, the cells were cultured in RPMI 1640 supplemented with 10% FCS, 50 mM 2-mercaptoethanol, 100 mM sodium pyruvate, 100 U/mL penicillin, 100 mg/mL streptomycin, and 1000 U/mL recombinant Granulocyte/macrophage colony-stimulating factor and 250 U/mL recombinant interleukin-4 (both from PeproTech, Rocky Hill, NJ). On days 3 and 6 of the culture, the non-adherent granulocytes and B and T cells were gently removed by suctioning half of the media and fresh media with cytokines were added. The released immature, non-adherent to loosely adherent cells were collected on day 8 with the morphologic features typical of immature DCs. The day 8 culture of the cells was used as immature DCs.

To determine the toxicity of the HINPs upon exposure to DC, immature cells (5×10^5) were incubated with HINPs (1mg/mL) for 1 hour at 37°C in a humidified CO_2 atmosphere. After incubation, DCs were washed ($3\times$) with PBS to remove extracellular HINPs and then were subjected to the viability test using trypan blue staining.

Two-photon imaging

Two-photon imaging was performed using a LSM510 laser scanning microscope equipped with a Fluar 20×0.75 NA objective (Carl Zeiss, Inc., Thorwood, NY). Two-photon excitation was achieved with a Coherent Chameleon Ti:Sapphire laser tuned to 880 nm (Coherent Inc., Santa Clara, CA) and fluorescence was collected using the non-descanned detectors. Green autofluorescence and red quantum dot fluorescence were separated by a DCLP540 dichroic mirror (Chroma Technology Corp., Rockingham, VT) and detected through 500–545 nm (green) and 550–600 nm (red) bandpass emission filters (Chroma).

Optical imaging

The CRI Maestro system (CRi) was used for phantom, in vitro and in vivo imaging. For phantom and in-vitro imaging the objects were put into microcentrifuge tubes. Live animals were imaged using isoflurane anesthesia. Optimized sets of excitation and emission filters were used to obtain a maximized fluorescence signal and low background. The excitation filters were defined as follows: 465 nm – blue; 529 nm – green; 640 nm – red; 690 nm – deep red; and 735 nm – NIR. The emission filters were set as 580 nm – visible, and 800 nm – NIR.

MR imaging

In vivo MR imaging was performed in a horizontal bore 9.4T magnet (Magnex Scientific Ltd, Abingdon, UK) interfaced to a Varian Inova (Varian Systems, Palo Alto, CA) console. A 38 mm transmit-receive birdcage coil was used to transmit and receive RF signals (Doty Scientific, Columbia, SC).

A T2-weighted multi-slice fast spin-echo sequence was used with a respiration-gated variable TR (2–3 sec). The imaging plane was defined with a FOV = 25.6×25.6 mm, matrix size 256×256, and a slice thickness of 0.5 mm. A slice gap of 0.5 mm was used to reduce slice profile effects. This resulted in a voxel size of $100 \times 100 \times 500$ μm^3. An echo train length of four (ETL = 4) was used with a centric k-space ordering for an effective TE of 10 ms. It is worth noting that although longer TE might improve contrast, several other factors were taken into account in balancing the desire for T2-contrast given other challenges related to the imaging sequence and anatomy. We observed that susceptibility effects from air-tissue boundaries and fat-muscle boundaries appeared to unacceptably degrade the image at longer echo time spacing. Furthermore, a greater TE spacing and also a longer echo train introduced unacceptable blurring due to T2 decay that interfered with the location of labeled cells. Alternate k-space orderings with the central line of k-space moved to 20, 30, and 40 ms did indeed increase T2 contrast among the surrounding tissues.

However, it was thought the labeled cells were more visible in surrounding tissue at the shorter TE. Typically at higher field strength T2 and T2* of tissues are shorter, thus a 10 ms will appear as more T2-weighted at higher field than at lower field strengths. This is especially true for iron that at high field has a very short T2. Thus maximal contrast between labeled cells and surrounding tissue may occur at shorter TE times.

Mice were anesthetized with 1.5% isoflurane delivered in O_2 at 2.5 L / min in accordance with IACUC protocol guidelines. The animal temperatures were monitored via rectal thermometer coupled to a continuous warm air feed to the magnet bore to assist in maintaining body temperature near 36° C throughout the experiment. Animal respiration was monitored via pillow sensor and the resulting signal utilized in respiratory gating.

MR imaging was performed prior to and 24 hours post injection of one million HINP-labeled DCs into the hind footpad of each animal. The contrast-to-noise as ratio was measured for each region of interest (ROI), using the formula contrast-to-noise ratio such as $(ROI_{fat} - ROI_{LN})/SD_{noise}$. Signal-to-noise ratios were measured for the LNs according to the relation of signal-to-noise ratio = SI_{org}/SD, where SI_{org} represents the signal intensity of the organ and SD is the SD of background noise. The contrast generated by T_2-weighted signal was compared using ImageJ software (National Institute of Health, Bethesda, MD).

Histology analysis of the migration of HINP-labeled DCs to the lymph nodes

After completion of the in vivo imaging experiments, the animals were sacrificed and the obviously swollen popliteal LNs were excised. Volume was measured using the formula $V = 4/3 \pi(r)^3$ with r as the radius. The LNs were then cut in half for Prussian blue staining or immunohistochemistry. For Prussian blue staining, the LNs were soaked in 10% formalin for 4–5 hours followed by overnight treatment with 70% ethanol. Afterward, the samples were embedded in paraffin and sliced. Once deparaffinization was complete, the slides were placed in a mixture of 2% potassium ferrocyanide and 2% hydrochloric acid for 20 minutes at 60°C. Following three washes with distilled water, the slides were counterstained with 0.1% nuclear fast red for 5 minutes. Finally, the slides were dehydrated in 95% ethanol. The iron distribution was determined by light microscopy.

For the CD11c immunohistochemistry of DCs in the LN, the samples were first snap frozen in liquid nitrogen. Five-micrometer sections of the frozen LN tissues were placed on charged slides. The slides were then treated with hydrogen peroxide to neutralize any endogenous peroxidases and treated with a UV block (Lab Vision, Fremont, CA) for 5 minutes to block any nonspecific staining prior to primary antibody addition. Then, the slides were incubated with affinity-purified hamster anti-CD11c antibody (eBioscience), diluted 1:200 for 6 minutes, followed by treatment with the Vectastain ABC Elite system (Vector Laboratories, Burlingame CA) and 3,3'-diaminobenzidine (Dako, Carpinteria, CA) to produce localized, visible staining. Finally, the slides were counterstained with Fast Green (Dako). All sections were visualized using a Zeiss Axioskop 40 microscope (Carl Zeiss MicroImaging, Thornwood, NY) equipped with AxioCam (Carl Zeiss MicroImaging) for digital images with a 40× objective lens.

Statistical analysis

The statistical significance of the differences between sample means was determined by Student's t test and the results were considered significant when P<0.05 with GraphPad Prism software.

Results

Design and development of HINPs

Besides the objective of developing HINPs for optical and MR imaging, we aimed to functionalize two versions of QDs including the visible and NIR QDs on the surface of SPIO. While the former can be used for optical imaging of DC migration using high resolution techniques, such as two-photon microscopy. The latter can be useful in tracking cell migration in a more global fashion. Among the library of QDs developed in our laboratory, the visible CdTe/CdS/ZnS and NIR CdHgTe/CdS/ZnS QDs exhibit physical properties that are well suited for cell imaging including major requirements such as water solubility, stability, precisely tunable emission wavelength, and high quantum efficiency. As shown in Figure 1, CdTe/CdS/ZnS and CdHgTe/CdS/ZnS QDs demonstrated distinct visible and NIR photoluminescence suitable for two-photon microscopy and optical NIR imaging, respectively. The quantum yields of the synthesized QDs were in the range of 20–50% with reference to Rhodamine 6G. The full width half maxima were 38 and 98 nm for visible and NIR QDs, respectively. Both the visible and NIR QDs are comparable in size and with an overall size that is slightly smaller than 5nm (Figure 2), they are ideal for use in coating much larger SPIO nanoparticles.

The synthesized QDs are stable under various buffer conditions. The MPA-stabilized CdHgTe/CdS/ZnS particles demonstrated superior stability compared to CdHgTe/CdS QDs (Figure S1). while MPA-stabilized QDs showed excellent stability in PBS as well as in NaCl; on the contrary, its predecessor, CdHgTe/CdS degraded notably under similar buffer conditions (Figure S1).

The central core of the HINP comprised of magnetic nanoparticles designed for MR imaging. This core is made of dextran-coated SPIO (SPIO-DX). The mean diameter of the iron oxide was in the range of 8–10 nm with a relatively narrow size distribution (Figure S2). After coating with dextran, the overall size increased approximately 30 nm[13]. Similar to the QD nanoparticles, SPIO-DX formed well dispersed and stable aqueous colloidal solutions under a variety of buffer conditions.

The design of the HINP assembly procedure was based on the electrostatic interactions between cationic and anionic counterparts described in the past[24, 25]. Specifically, the technique consists of a sequential deposition of charged cationic and anionic parts to build up the multilayer structure[26]. Regarding the SPIO core, as we analyzed the zeta potential under various pH conditions (Figure 3A), it was apparent that the surface was occupied primarily by dextran-generated negative charge. It is worth noting that the SPIO-DX nanoparticles were quite stable, and that its size remained unchanged upon exposure to various pH conditions. Next, SPIO-DX nanoparticles were coated with a charged polyelectrolyte (PE), such as PAH, to create a net positive charge on the surface. Aside from generating a counter ion for association with the negatively charged MPA-stablized QDs, the PAH served as a buffer zone to minimize the quenching effect due to the proximity of the QDs to the iron oxide core of SPIO[19, 27]. Therefore, separating the magnetic and fluorescent counterparts using PE layer could help retain high photoluminescence.

The association of PAH with SPIO-DX resulted in an increase in the overall size of the final product, referred to hereafter as SPIO-DX-PAH nanoparticles. This increase in the size of the particles was inversely proportional to the zeta potential (Figure 3B). Fine-tuning the coating process can be controlled to achieve the desired size according to the pH and ionic strength of the buffers[28]. During the course of work, we preferred to assemble the PAH layer at pH5 in saline which afforded SPIO-DXPAH nanoparticles that were approximately 65 nm and had a zeta potential of 8.2 mV.

We employed QCM technique to gather quick information regarding the coating step. As shown in Figure S3, each coating step was verified by measuring the frequency shift. This drop in frequency demonstrated that the weight of assembled probes increases with each coating step. Finally, the HINP was obtained by tethering negatively charged QDs with the positively charged SPIO-DX-PAH nanoparticles. To generate the fluorescent component for multimodal imaging, both the visible and NIR QDs were used to coat the SPIO-DX-PAH particles. Successful synthesis of the HINP was evidenced by the increased size of the particles to approximately 123 nm (Figure 4A). For each step in the modification, the charge on the surface of the particles was alternated in accordance with the coating materials (Figure 4B). No registered dissociation of QDs from HINP was noted when the HINP was formed, thus indicating the stable attachment of QDs within the probe. We were able to confirm the specificity of attraction between the two oppositely charged entities, using control experiments such as mixing QDs with SPIO-DX nanoparticles in one solution. As evidenced by DLS analysis, however, this mixing did not lead to the association of QDs with SPIO-DX.

In the previous study, we demonstrated that PLL could be used as a transfecting reagent for shuttling the SPIO probe inside DCs[13]. In this work, we decided to derivatize PLL on the outer layer to stabilize the HINP and enhance cell membrane permeability. The final coating of HINP with PLL led to size enhancement and a change in surface charge (Figure 4). The topography of the HINP product compared to the starting material of SPIO-DX can be seen in AFM images (Figure S4). The HINP appeared as nearly round particles, with the diameter enlargement resulting from the multilayer fabrication. This observation is in line with the reported DLS analysis data.

The optical integrity of the HINP was assessed by collecting the absorption spectra. The presence of both visible and NIR QDs in HINP was evidenced by the maxima absorption peaks, which occurred at 600 and 800 nm (Figure S5). The immobilized QDs on the superparamagnetic iron core were tested by illuminating the HINP using UV light, at the same time, the probe can be aggregated and redispersed upon exposing to or removing the probe from a magnetic source (Figure S6). Furthermore, we tested the fluorescence signal of each QD in the HINP by examining their respective excitation/emission wavelengths. The fluorescence signal detected from HINP contained unique emissions as detected by two different filters set at 580 and 800 nm (Figure S7). To confirm that our observation was not due to signal bleaching from one channel to another, we decided to develop control probes into which we incorporated either visible- or NIR-QDs onto the SPIO and tested their fluorescence. We did not see any signal interference in the filter set used in our work (data not shown). Taken together, the HINP's fluorescence signal is stable, and as we measured the sample over the course of several days, we did not observe any signal loss or drift in signal intensity.

Discussion

One of the critical barriers in cell therapy is that the distribution of cells in vivo is poorly defined. After adaptively transferring the DCs to the host, little information exists regarding how and where and if the cells can migrate after vaccination or what is the cellular fate in vivo. Effective migration of DCs from the injection site to the secondary lymphoid tissue is crucial for antigen presentation and successful therapy. Understanding this mechanism would contribute significantly to the new knowledge in cell therapy. Toward that goal, in this work, we developed a multimodal probe for tracking DC migration in vivo. The HINP was comprised of visible and NIR emitting semiconductor quantum dots (QDs) tethered to SPIO nanoparticles. Furthermore, the HINP was incorporated with PLL on the surface to enhance cell membrane permeability.

To test the ability of HINP to report the migration of cells in vivo, DCs were incubated with HINP for one hour using the same procedure reported previously[13, 23]. First, however, we assessed the toxicity of HINP compared to each of the separate components such as SPIO-DX, SPIO-DX-PAH, and QDs alone. Interestingly, we observed that all are safe; except that SPIO-DX has an unrecognized toxicity and the rest caused some 6–8% of cell death, a rate within acceptable limits given the high dose used in this work[29]. HINP-labeled DCs were injected into the footpads of mice (n=5), and the resultant fluorescence signal was observed in the feet using optical imaging (Figure 5A). At 24 hours post injection, we observed decreased signal intensity, which suggested that some of the labeled DCs may have migrated deep inside the tissue. The migration and homing of the labeled DCs was confirmed by MRI (data not shown). Next, we quantified the signal reduction in the popliteal LNs using MRI. Here, mice (n=3) were injected in one footpad after which we imaged cell trafficking in the popliteal LN using a 9.4T scanner. The advantages of using a single animal to compare the signal using MRI are that the process is easy to control and monitor, and it reduces the effects of animal-to-animal variability. The MR images revealed that HINP-labeled DCs in the LN caused significant LN swelling and a reduction in T2-weighted signal intensity compared to the signal obtained from the other symmetrical LN (Figure 5B). Quantitatively, mean post-contrast signal intensity decreased significantly from 127.005 ± 7.82 to 83.409 ± 5.234 (P < 0.01). Immediately after MR imaging, the popliteal (LNs) were surgically exposed for imaging using two-photon microscopy (n=3). As expected, the HINP-labeled DCs were detected in the LNs via an abundant fluorescence signal (Figure 6A). To confirm that the signals obtained from MRI and two-photon microscopy indeed came from the labeled DCs, the LNs were dissected and stained for iron and CD11c using Prussian blue and immunohistochemistry, respectively. On average, LNs from treated mice have a volume of approximately 10.35 mm^3 ± 2.54 compared to 0.75 mm^3 ± 0.32 from the control LNs (P < 0.0089). We observed a modest infiltration of the labeled cells in LNs; interestingly, most of the signals were in the margin of the LNs (Figure 6 B, C).

In conclusion, we have reported the development and application of a hybrid nanoprobe comprised of well characterized visible and NIR QDs and SPIO nanoparticles coated with a transfecting reagent. Such a probe might be used for many imaging applications including cell tracking and the imaging of biological targets in different types of disease models. Considering the stability of the nanocomposites and the quantum stability of QDs compared to organic dyes such as cyanine dyes, the probe offers excellent characteristics for chemical modification, long shelf life and suitability for imaging targets that require longitudinal tracking migration. Aside from this cell tracking study, we envision that the hybrid technology described in this work will provide a suitable basis for maintaining an adequate circulation half-life in vivo, thus potentially yielding a longer residence time at the target site, a characteristic that would further enhance the contrast signal.

Supplementary Material

Refer to Web version on PubMed Central for supplementary material.

Acknowledgments

References

1. Achilefu S, Jimenez HN, Dorshow RB, et al. Synthesis, in vitro receptor binding, and in vivo evaluation of fluorescein and carbocyanine peptide-based optical contrast agents. J Med Chem. 2002; 45:2003–15. [PubMed: 11985468]

2. Jaffer FA, Tung CH, Gerszten RE, Weissleder R. In vivo imaging of thrombin activity in experimental thrombi with thrombin-sensitive near-infrared molecular probe. Arterioscler Thromb Vasc Biol. 2002; 22:1929–35. [PubMed: 12426227]

3. Jaffer FA, Tung CH, Wykrzykowska JJ, et al. Molecular imaging of factor XIIIa activity in thrombosis using a novel, near-infrared fluorescent contrast agent that covalently links to thrombi. Circulation. 2004; 110:170–6. [PubMed: 15210587]

4. Law B, Weissleder R, Tung CH. Protease-sensitive fluorescent nanofibers. Bioconjug Chem. 2007; 18:1701–4. [PubMed: 17915958]

5. Quinti L, Weissleder R, Tung CH. A fluorescent nanosensor for apoptotic cells. Nano Lett. 2006; 6:488–90. [PubMed: 16522048]

6. Tung CH, Bredow S, Mahmood U, Weissleder R. Preparation of a cathepsin D sensitive near-infrared fluorescence probe for imaging. Bioconjug Chem. 1999; 10:892–6. [PubMed: 10502358]

7. Ye Y, Bloch S, Xu B, Achilefu S. Design, synthesis, and evaluation of near infrared fluorescent multimeric RGD peptides for targeting tumors. J Med Chem. 2006; 49:2268–75. [PubMed: 16570923]

8. Bogdanov A Jr. Matuszewski L, Bremer C, Petrovsky A, Weissleder R. Oligomerization of paramagnetic substrates result in signal amplification and can be used for MR imaging of molecular targets. Mol Imaging. 2002; 1:16–23. [PubMed: 12920857]

9. Chen JW, Pham W, Weissleder R, Bogdanov A Jr. Human myeloperoxidase: a potential target for molecular MR imaging in atherosclerosis. Magn Reson Med. 2004; 52:1021–8. [PubMed: 15508166]

10. Dodd SJ, Williams M, Suhan JP, Williams DS, Koretsky AP, Ho C. Detection of single mammalian cells by high-resolution magnetic resonance imaging. Biophys J. 1999; 76:103–9. [PubMed: 9876127]

11. Pop M, Sermesant M, Lepiller D, et al. Fusion of optical imaging and MRI for the evaluation and adjustment of macroscopic models of cardiac electrophysiology: a feasibility study. Med Image Anal. 2009; 13:370–80. [PubMed: 18768344]

12. Sosnovik D, Weissleder R. Magnetic resonance and fluorescence based molecular imaging technologies. Prog Drug Res. 2005; 62:83–115. [PubMed: 16329255]

13. Kobukai S, Baheza R, Cobb JG, et al. Magnetic nanoparticles for imaging dendritic cells. Magn Reson Med. 2010; 63:1383–90. [PubMed: 20432309]

14. Qian H, Dong C, Peng J, Qiu X, Xu Y, Ren J. High-quality and water-soluble near-infrared photolumineseent CdHgTe/CdS quantum dots prepared by adjusting size and composition. Journal of Physical Chemistry C. 2007; 111:16852–7.

15. Rogach AL, Kotov NA, Koktysh DS, Susha AS, Caruso F. II-VI semiconductor nanocrystals in thin films and colloidal crystals. Colloids and Surfaces, A: Physicochemical and Engineering Aspects. 2002; 202:135–44.

16. Wang Y, Tang ZY, Correa-Duarte MA, Pastoriza-Santos I, Kotov NA, Liz-Marzan LM. Photoactivation of citrate-stabilized CdSe and CdSe@CsS core-shell nanoparticles: Mechanism of enhancement of quantum yield. Abstr Pap Am Chem S. 2004; 228:U866–U.

17. Fang Z, Li Y, Zhang H, Zhong XH, Zhu LY. Facile Synthesis of Highly Luminescent UV-Blue-Emitting ZnSe/ZnS Core/Shell Nanocrystals in Aqueous Media. Journal of Physical Chemistry C. 2009; 113:14145–50.

18. Yan CM, Tang FQ, Li LL, et al. Synthesis of Aqueous CdTe/CdS/ZnS Core/shell/shell Quantum Dots by a Chemical Aerosol Flow Method. Nanoscale Research Letters. 2010; 5:189–94. [PubMed: 20652095]

19. Hong X, Li J, Wang MJ, et al. Fabrication of magnetic luminescent nanocomposites by a layer-by-layer self-assembly approach. Chemistry of Materials. 2004; 16:4022–7.

20. Jin Y, et al. Plasmonic fluorescent quantum dots. Nat Nanotechnol. 2009; 4:571–6. [PubMed: 19734929]

21. Grant GG, Koktysh DS, Yun B, Matts RL, Kotov NA. Layer-By-Layer Assembly of Collagen Thin Films: Controlled Thickness and Biocompatibility. Biomedical Microdevices. 2001; 3:301–6.

22. Sinani VA, Koktysh DS, Yun BG, et al. Collagen coating promotes biocompatibility of semiconductor nanoparticles in stratified LBL films. Nano Letters. 2003; 3:1177–82.

23. Pham W, Xie J, Gore JC. Tracking the migration of dendritic cells by in vivo optical imaging. Neoplasia. 2007; 9:1130–7. [PubMed: 18084620]

24. Hong X, Li J, Wang M, et al. Fabrication of magnetic luminescent nanocomposites by a layer-by-layer self-assembly approach. Chem Mater. 2004; 16:4022–7.

25. Zebli B, Susha AS, Sukhorukov GB, Rogach AL, Parak WJ. Magnetic targeting and cellular uptake of polymer microcapsules simultaneously functionalized with magnetic and luminescent nanocrystals. Langmuir. 2005; 21:4262–5. [PubMed: 16032831]

26. Decher G, Hong JD. Buildup of Ultrathin Multilayer Films by a Self-Assembly Process .1. Consecutive Adsorption of Anionic and Cationic Bipolar Amphiphiles on Charged Surfaces. Makromol Chem-M Symp. 1991; 46:321–7.

27. Corr SA, Rakovich YP, Gun'ko YK. Multifunctional magnetic-fluorescent nanocomposites for biomedical applications. Nanoscale Research Letters. 2008; 3:87–104.

28. Aulin C, Varga I, Claessont PM, Wagberg L, Lindstrom T. Buildup of polyelectrolyte multilayers of polyethyleneimine and microfibrillated cellulose studied by in situ dual-polarization interferometry and quartz crystal microbalance with dissipation. Langmuir. 2008; 24:2509–18. [PubMed: 18278961]

29. Singh N, Jenkins GJS, Asadi R, Doak SH. Potential toxicity of superparamagnetic iron oxide nanoparticles (SPION). Nano Reviews. 2010; 1:5358–72.
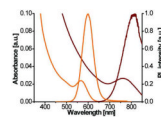
Figure 1.
Normalized absorption and photoluminescent spectra of water soluble visible (orange) and NIR (brown) QDs.
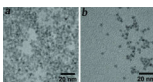
Figure 2.
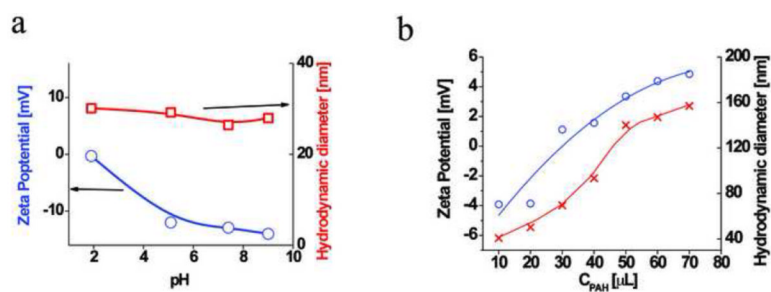High resolution TEM images of water soluble visible (a) and NIR (b) QDs.

Figure 3.
(a) Zeta potential (●) and hydrodynamic diameter (□) of dextran-coated SPIO nanoparticles under various pH conditions; (b) Zeta potential (●) and hydrodynamic diameter (X) of SPIO-DX coated with PAH at pH 7.4.
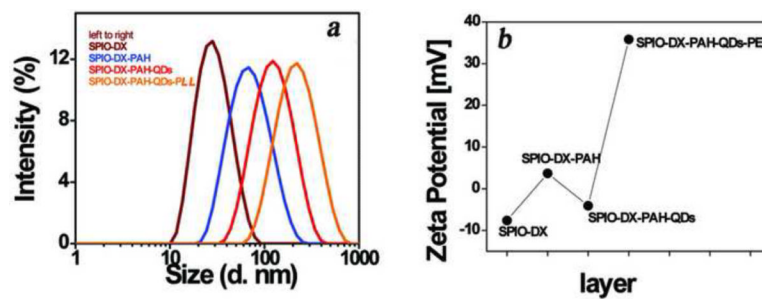
Figure 4.
The hydrodynamic diameter of HINP at different stages of fabrication (a). The overall size of the product increased additional layers of the coating process were achieved. The shifting of the charge on the surface of nanoparticles in every step of the synthesis (b).
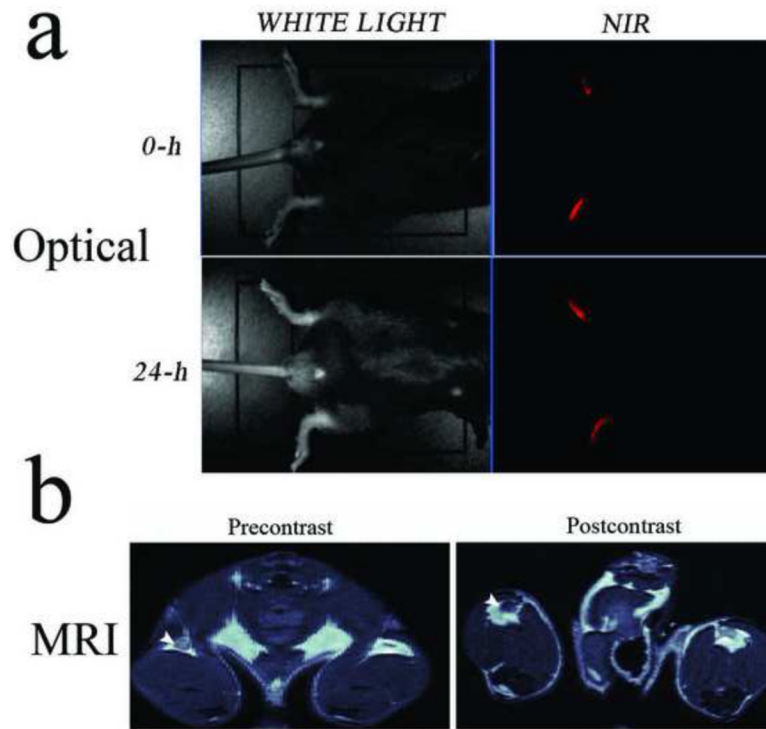
Figure 5.
Multimodal imaging of cell migration. Optical imaging of syngeneic mouse with HINP-labeled DCs injected in the footpads. The scan was performed right after injection and 24-h post injection (A). In vivo MR imaging of mice 24-h post injection of the HINP-labeled DCs in the footpad. The postcontrast signal intensity of the right popliteal LN (arrowhead) appears darker compared to the signal from the precontrast, indicating the presence of DCs (B).
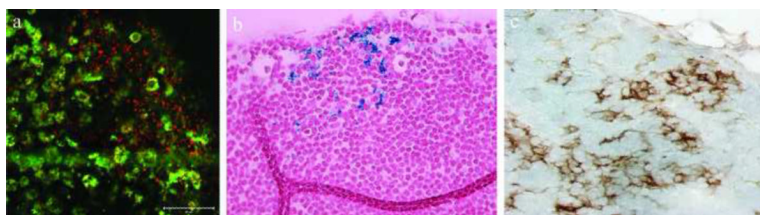
Figure 6.
Two-photon microscopy of migrated HINP-labeled DCs (red) to the popliteal LN; autofluorescence (green) (scale bar 50 μm) (A); Iron and immunohistochemical (CD11c) staining, both at 40× (B, C).